Attribution of Fano resonant features to plasmonic particle size, lattice constant, and dielectric wavenumber in square nanoparticle lattices

Drew DeJarnette,[1] Justin Norman,[2] and D. Keith Roper[1,2,*]

[1]*Microelectronics and Photonics Graduate Program, University of Arkansas, Fayetteville, Arkansas 72701, USA*
[2]*Department of Chemical Engineering, University of Arkansas, Fayetteville, Arkansas 72701, USA*
**Corresponding author: dkroper@uark.edu*

Received August 20, 2013; revised November 12, 2013; accepted November 12, 2013;
posted November 15, 2013 (Doc. ID 194949); published January 6, 2014

Fano resonances between plasmons and diffracted light offer tunable energies and locales, but attribution of Fano resonance features to geometry and physicochemistry of metal nanostructures and adjacent dielectrics has been confounded by complexity and computational expense. This work shows predictable modal shifts of Fano resonance in square lattices of plasmonic nanostructures can be attributed directly to changes in medium wavenumber, particle size, and lattice constant that alter plasmon polarizability and diffractive interference. For 45 to 80 nm radius particles, a window of lattice constants that support Fano resonances is identified in a range from 500 to 900 nm. Lattice constants that support high intensity resonances are determined by individual particle polarizability and medium wavenumber. Fano resonance wavelengths redshift from diffracted photon energies as local refractive index (RI) changes due to coupling with particle polarizability in the window. Redshift sensitivities for quadrupole, dipole, and Fano resonances are 150, 348, and 541 nm, respectively, per RI unit. Fano resonance intensity may be enhanced more than tenfold by selecting nanoparticle sizes and lattice constants. The quantitative effects of such parametric changes are rapidly and intuitively distinguished using a semi-analytic approach, consisting of an exact expression for particle polarizability, a trigonometric description of diffraction, and a semi-analytical coupled dipole approximation.

OCIS codes: (230.5298) Photonic crystals; (250.5403) Plasmonics; (290.5850) Scattering, particles; (050.1755) Computational electromagnetic methods.
http://dx.doi.org/10.1364/PRJ.2.000015

1. INTRODUCTION

Controlling light–matter interactions using plasmon nanostructures relies on amplification of harmonic oscillation in a metal–dielectric system by facile transfer of energy between different stored forms. Harmonic amplification results in familiar mechanical, acoustical, or optical resonances. Two distinct physical systems that oscillate at a common frequency can couple to intensify the individual oscillations creating a resonance. For example, coupling between continuous incident light and broadband atomic or molecular vibrations yields characteristic scattering or absorbance resonances such as visible blue spectra for atmospheric molecules. Such resonances generally exhibit a symmetric lineshape about a modal coupling frequency and are described as Lorentzian or Gaussian, depending on the involved parameters. However, when broadband or continuum oscillation such as white light couples with narrow, discrete band resonances such as from metal diffraction gratings, an asymmetric lineshape appears, as reported first by Wood [1].

The theoretical framework describing the asymmetric coupled resonances was subsequently developed by Fano in the context of quantum mechanical systems [2]. Fano examined asymmetric autoionization from electron scattering resulting from interaction between a resonant, discrete atomic electronic state and a background continuum of atomic states. Since its initial treatment in quantum systems, Fano resonance coupling has been identified in a number of contexts. One example is coupling between narrow Bragg diffraction [3] from ordered nanosized nodes of two-dimensional (2D) photonic crystals [4,5] and broad scattering from plasmon-active nanoparticles originally described by Mie [6]. An asymmetric transmission spectrum indicative of Fano resonance interaction is observed from such systems [7–9]. Growing interest in predicting the optical and photonic behavior of an artificial 2D photonic crystal, one of a broader class of metamaterials, motivates deepened understanding about how the physical attributes of its constituent meta-atoms affect resulting Fano resonance features.

In plasmonic systems considered to date, Fano resonances have been generated by coupling between plasmons and either multipolar or diffractive modes in nanostructures [10–22]. Fano resonances resulting from coupled plasmons are reviewed in Ref. [20]. The effects of fundamental electrodynamics arising from metamaterial characteristics on spectroscopic Fano resonance features in these systems were described using analytic expressions [10–15] as well as numerical simulation [16–19]. Table 1 categorizes these studies by the type of description used and by the near- or far-field origin of the Fano resonance.

Near-field analytic and numerical descriptions predominate due to interest in refining local structures of nanoelements to enhance light manipulation. Previous analytical descriptions provide insight into physical mechanisms supporting Fano

Table 1. Categorization of Select, Recent Studies of Fano Resonant Plasmonic Nanostructures According to Source and Type of Description

	Analytic	Numerical
Near-field	[10–15]	[16–19]
Far-field	[15,21]	[22]

resonances, but often have small windows of applicability and/or require fitting of parameters. Prior numerical descriptions allow quantitative evaluation with broader applicability, but computation can obscure intuitive insights and computational expense limits evaluation of complex and/or multicomponent systems. Reported far-field descriptions examine key features supporting Fano resonances, such as alterations in local and/or periodic properties that support cloaking or flat lensing. However, computational expense has prevented evaluation of these features for complex systems or across broad changes. Interactive effects between photon diffraction, polarizable inclusions, and changes in local dielectric values, in particular, have not been examined in detail.

Physical and geometric features affecting near- and far-field interactions supporting Fano resonance features that have been evaluated singly include background dielectric constant [15] and inclusion of the substrate for asymmetric cladding [23]. The dielectric constant of media between neighboring plasmonic structures can maximize resonant coupling in quantum computing [24,25], terahertz (THz) transmission and generation [26,27], biological imaging [28,29], light trapping and modulation [30–32], photovoltaics [33,34], resonance shifting for sensing [7,8,35,36], nanoscale distance changes [37,38], control of incident polarization [39], and detection of graphene [40].

This work explicitly attributes the effects of physical (dielectric constant) and geometric (radii, spacing) characteristics of 2D photonic crystal lattices of subwavelength metal nanoparticles on particular spectral features (energy, bandwidth, amplitude, and sensitivity) of Fano resonances. Trigonometrically defined coherence in oscillatory interference of Bragg diffraction is shown to be a necessary, but insufficient, condition to support far-field Fano resonance. Such coherent interference gives rise to resonance in nanoantennas at frequency values that can be tuned by antenna geometry as well as local sub- and super-strate dielectric constants [7,8,41,42]. Particle polarizability, a measure of electron inducibility in plasmon oscillation, and a geometric array parameter that defines lattice scattering are both shown to be determined by the medium wavenumber. Using refined trigonometric [41] and coupled dipole approximation [42] descriptions, redshifts in Fano resonance energy are directly related to changes in lattice geometry, radius-dependent nanoparticle polarizability, and reradiation. In particular, increasing refractive index (RI) of the intervening dielectric is shown to redshift Fano resonance spectra from geometric interference patterns. Individual particle plasmon resonance is shown to broaden and shift with increasing RI, requiring optimization of array parameters at each particle environmental condition. Intuitive results are obtained using an expression for plasmon electrodynamics in a symmetric semi-analytic description of far-field scattering that supports *a priori* attribution of effects of size, composition, and spacing of subwavelength meta-atoms as well as dielectric composition of intervening media on spectral features of the unique Fano resonance supported by this 2D metamaterial.

2. MATERIALS AND METHODS

Spectral responses of nanoparticle ensembles were computed using a rapid semi-analytic coupled dipole approximation (rsa-CDA) [41,42]. This formulation treats each nanoparticle as a single point dipole with dipole polarizability, α. Nanoparticles were arranged in a 2D square lattice. The formulations are based on an infinite lattice, which reduces computational expense and provides insight into underlying physical interactions. Incident irradiation was orthogonal to the lattice and polarized parallel to a selected coordinate axis. Extinction was calculated using Eq. (4) in [42]. Attribution of Fano resonance shifts to medium wavenumber was based on a homogenous dielectric matrix existing between elements of the lattice.

Attribution of shifts in plasmonic behavior from changes in the intervening dielectric RI were interpreted by visualizing changes in nanoparticle polarization. In linear materials such as noble metals (such as Au, considered here), particle polarization, **P**, is proportional to the electric field at each dipole with particle polarizability, α, being the constant of proportionality. In the rsa-CDA for an infinite 2D square lattice of dipoles [8,42], effects of RI are embedded in α, which defines the plasmonic behavior of nanoparticles and determines relative amounts of absorption and scattering that are key in attributing Fano resonance behavior. Change in nanoparticle polarization caused by wavelength contraction is illustrated in Fig. 2 for two different RI values using the same incident energy. It is apparent that a longer wavelength would be required in higher dielectric η_2 to maximize natural resonance of a nanoparticle, relative to that required in a smaller dielectric η_1. In illuminated conductors, "free" electrons having no binding energy associated with them oscillate in response to the incident field as described by the conductivity of the material. Since the size of particles considered in this work is within the scattering regime, nonlocal effects are neglect and optical properties for Au were taken from [43]. Increasing RI in the intervening dielectric causing wavelength contraction can induce higher-order electric modes such as the quadrupole. The quadrupole mode, one such higher-order mode, was also examined using particle polarizability, which is valid for special cases [42,44,45].

The effects of particle size, composition, and intervening dielectric RI of the lattice on spectral features were evaluated using an analytic expression for single particle polarizability. The case of spheres is considered here due to the availability of analytic expressions for both polarizability and far-field interactions from point dipoles, i.e., the retarded dipole sum. The polarizability can be expressed as separate dipole and quadrupole terms, respectively, by

$$\alpha_d = 4\pi\left(\frac{3iR^3}{2x^3}a_1\right), \quad \text{and} \quad \alpha_q = 4\pi\left(\frac{10iR^3}{3x^3}a_2\right), \tag{1}$$

where R is the particle radius, $x = kR$ is a size parameter, with k being the η-dependent medium wavenumber defined above,

and a_i are the Mie coefficients, which are functions of x and the ratio of RIs of the particles to the medium [42]. Dipole and quadrupole modes appear as individual treatments of each term in Eq. (1). Although obscured here in the Mie coefficients, plasmon resonance occurs when the a_i term diverges at values of $m^2 + i^{-1}(i+1)w_i$, where m is the ratio of RI values inside to outside the nanoparticle and w_i is a complex polynomial defined by Mie [42]. For particles much smaller than the incident wavelength, w_i approaches unity and the dipole ($i = 1$) mode dominates giving the familiar quasi-static resonance location of $m^2 = -2$. As an example, a sub-25-nm diameter Au nanoparticle would have a plasmon resonance when the frequency of incident light gives an Au dielectric function that has a real component of –2 for vacuum and 2.66 for water. Larger particles require solving Mie coefficients using Riccati–Bessel functions that obscure the direct comparison for small particles dominated by absorption. Graphical representation of Eq. (1) is shown in Section 4 to help elucidate the effects of RI on single particle plasmon resonance.

3. INTERVENING DIELECTRIC ALTERS DIFFRACTIVE MODE AND FANO RESONANT ENERGY

Figure 2 illustrates redshifts in Fano resonance (solid lines) wavelength from square nanoparticle lattices of dipole scatterers for medium RIs of 1.00 (black), 1.17 (blue), and 1.33 (red). Fano resonance peaks occur at lower energies than lattice scattering (dashed lines). Each Fano resonance spectrum is from a square lattice of 70 nm radius Au spheres. Redshifting results from both wavelength contraction and nanoparticle coupling. The frequency of oscillations in spectral features that result from diffractive interference decreases as RI and medium wavenumber increase.

Lattice scattering (i.e., phase overlap or diffractive interference; dashed lines) appears as an oscillatory, wavelength-dependent feature arising from constructive and destructive interference due to phase overlap between light reradiated from perfect, adjacent dipoles in the square 2D lattice. Three respective interference patterns were calculated trigonometrically following Ref. [41] in Fig. 2 at a common lattice constant of 600 nm for constant RI environments of 1 (black), 1.17 (blue), and 1.33 (red). The primary lattice scattering peaks occur at incident vacuum wavelength values a few nanometers larger than $\lambda = \eta D$ (i.e., lambda = 600 nm for the black spectra). These correspond primarily to axial contributions for all RI values. A secondary diffraction peak corresponding to half the diagonal distance occurs at $\lambda = \eta D/2^{1/2}$, which is only shown for the 1.33 (red-dotted) case at a wavelength value of 565 nm (red, hollow triangle). No Fano resonance occurs for this peak since the diffraction wavelength is blueshifted from the plasmon window. Similar results were shown by [15] using a heuristic Fano model for two discrete changes in particle spacing at a single RI value of 1.5. The peak values for lattice scattering correspond to first-order axial and second-order diagonal elements in the array, respectively. The peak values result from local electric field coherence, which enhances localized fields by the scattering particles due to constructive phase interference, as suggested by Ref. [46].

Extinction efficiency (i.e., Fano resonance; solid lines) supported by lattice scattering and plasmon oscillation in lattices of 70 nm radius gold (Au) nanoparticles was calculated in Fig. 2 using the rsa-CDA [41]. This plasmon-diffraction coupling excites a particular geometric mode from the underlying lattice scattering. Changing lattice spacing and particle size shifted these resonances, which in turn shifted the Fano resonance peak to different underlying geometric modes in the spectra. No Fano resonance occurs at the secondary (i.e., half diagonal) phase overlap because Fano resonance is not supported at values of incident wavelength less than the plasmon wavelength [15].

The respective extinction spectra in Fig. 2 have maximum Fano resonance locations marked by a black square (1.00), a blue circle (1.17), and a red triangle (1.33), respectively. Extinction energy decreases at higher RI as illustrated in the inset of Fig. 1. The intensity of extinguished light differs from the constructive interference intensity due to phase overlap. Redshifting of extinction maxima from the lattice constant multiplied by the RI arises due to coupling between plasmon oscillations and diffracted light. This radius-induced redshift has been observed using similar CDA [41,42,47], discrete dipole approximation (DDA) [48], and Fano profile models [21]. The inset enlarges the middle, blue spectra for RI of 1.17 to show correspondence between oscillations in lattice scattering and extinction efficiency. For the 600 nm lattice, the value of ηD is 702 nm. Wavelengths are shown from 700 to 750 on the abscissa, while extinction efficiency (solid) and phase overlap (dashed) are shown on left- and right-hand ordinate axes, respectively.

Oscillation frequency in phase overlap and far-field Fano resonance from array geometry in Fig. 2 vary with medium wavenumber. The dependence of both plasmon and diffractive modes on RI is explicit in the medium wavenumber, k, which is proportional to η of the intervening dielectric, i.e., the "medium" that contains the nanoparticle lattice. Figure 2 shows that increasing the lattice parameter, $A = kD$, by increasing η, decreases the rate of oscillation in both phase overlap as well as extinction spectra. The peak-to-peak wavelength differences in oscillation for RI = 1.00, 1.17, and 1.33

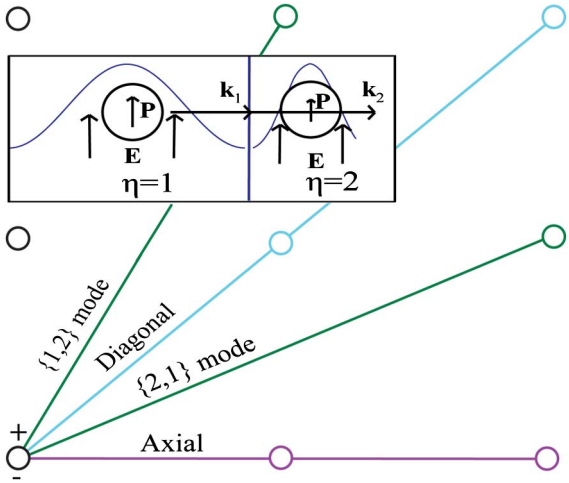

Fig. 1. Schematic of the square lattice of nanoparticles (hollow circles) identifying diffraction modes (solid lines) that constitute unique particle chains. Inset depicts wavelength contraction of a plane wave moving from a smaller to a larger index of refraction medium and its effects on nanoparticle polarizability. Incident energy that excites resonance at η_1 must be reduced to excite resonance at $\eta_2 > \eta_1$.

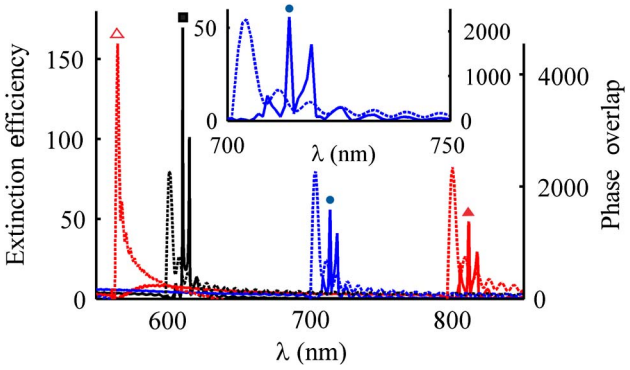

Fig. 2. Phase overlap (dashed line) onto a center particle was calculated using Ref. [41] for a lattice constant of 600 nm and RI values of 1.00 (black; peak ~600 nm), 1.17 (blue; ~700 nm), and 1.33 (red; ~800 and 575 nm). Extinction spectra (solid line) were calculated by rsa-CDA for corresponding infinite arrays of 70 nm radius Au particles with lattice constant 600 nm. The inset expands the 1.17 RI array to show that constructive interference from lattice scattering supports extinction peaks.

were 6.5, 7.5, and 8.75 nm, respectively. Increased peak-to-peak distances at larger RIs result from diminishing effects of lowering incident energy at higher RI. For comparable ratios of ηD and λ, increases in λ away from ηD have a smaller effect on the ratio $\eta D/\lambda$, when the numerator is larger.

Comparing lattice scattering and extinction efficiency in Fig. 2 inset distinguishes the effects of interfering phase overlap from polarizability-induced extinction, showing that both array and particle geometry impact far-field Fano resonances. This supports the design of systems with highly sensitive Fano features for applications in sensing, or insensitive Fano features for devices that require robust and consistent optical response. The far-field effects on Fano resonance examined in this work extend previous results [14] in which near-field coupling interaction between two different plasmon modes supporting a Fano resonance were modified by manipulating near-field interactions with a double layer nanowire assembly. This work evaluates the additional effects of wavelength and lattice dimensions on both near- and far-field features of Fano resonances. This additional degree of freedom furthers design of physical and geometric features of plasmon-active nanoparticles and their lattices to achieve particular spectral outcomes of these 2D metamaterials.

4. INTERVENING DIELECTRIC REDSHIFTS AND BROADENS SINGLE PARTICLE PLASMON RESONANCE ENERGY AND BANDWIDTH

Figure 3 illustrates that the broadband plasmon resonance that underlies Fano extinction expands and redshifts when isolated particles are excited in media of increasing RI (i.e., water versus vacuum). The imaginary component of polarizability shown in Fig. 3 was calculated using Eq. (1) for particle radii from 25 to 80 nm and incident wavelengths from 400 to 900 nm. It exhibits a dipole resonance (solid arrow) alone at vacuum RI for these particle sizes. An additional quadrupole resonance (hollow arrow) appears at aqueous RI. The changes in polarizability with RI affect the energy and bandwidth of dipole and quadrupole resonances for isolated particles as shown in Fig. 4. This is illustrated in Fig. 4 for a

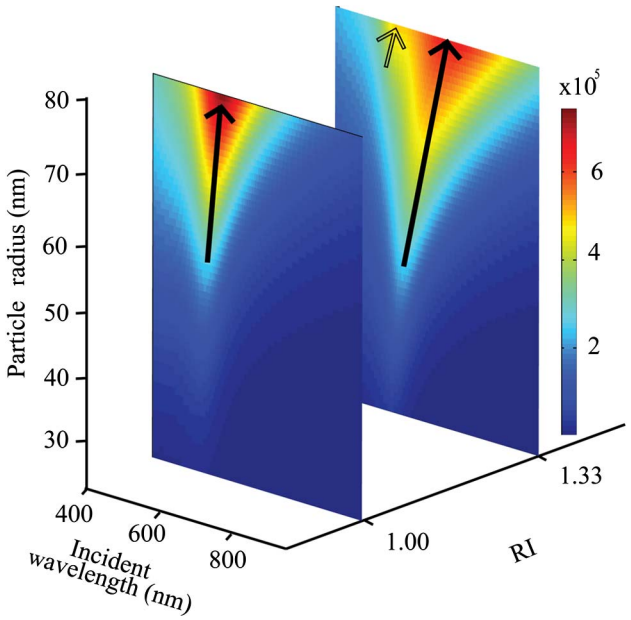

Fig. 3. Imaginary component of particle polarizability [Eq. (1)] is shown as the color gradient for RI values of 1.00 and 1.33 over a range of particle sizes and incident vacuum wavelength values.

70 nm radius Au nanoparticle at three different RI values using both the polarizability model and Mie theory.

Energy shifts and broadening in plasmon resonance as the intervening dielectric changes are not solely a result of wavelength contraction. Radiative losses and molecular polarization of the intervening dielectric in response to the local charge density of the oscillating plasmons in the nanostructure act as dampeners to the Coulombic restoring force. This is accounted for in the polarizability model in Eq. (1). The net result is a nonlinear redshifting and broadening of the resonant dipole, quadrupole, and higher-order electric modes with respect to the vacuum plasmon wavelength [49] as shown in Fig. 3. Changes in these modes result in redshifting and broadening of the Fano resonance as shown in Fig. 2. The polarizability of isolated nanostructures determines relative amounts of radiation (i.e., scattering) and absorption, as well as the wavelength (frequency) of maximum scattering. The effects of such plasmon shifts on the Fano resonance of split-ring designs have been observed with graphene [40].

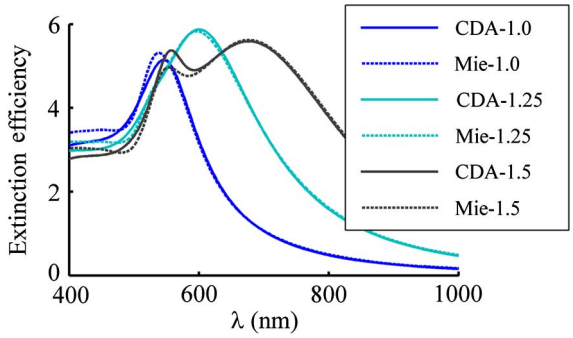

Fig. 4. Comparison of single particle extinction spectra calculated for 70 nm radius spherical particles using the exact Mie theory (dotted) and the dynamic dipole polarizability (solid lines) with the quadrupole extension. The homogeneous RI surrounding each particle is shown in the legend.

Redshifting of plasmon maxima as well as expanded bandwidth appears in Fig. 3 as particle size increases. Increasing RI to 1.33 enhances these affects and induces a higher-energy quadrupolar activity (hollow arrow) for particle radii >70 nm. These energy shifts and higher-order electric modes from increased RI enhance Fano resonant behavior at smaller particle sizes and provide larger bandwidth for tunable device design. For example, a 60 nm radius particle has a maximum particle polarizability that redshifts from 594 nm at $\eta = 1.00$ to 632 nm at $\eta = 1.33$. The plasmon resonance for particles > about 40 nm radius is dominated by scattering. Field enhancements accrued by periodically ordering such particles support electron excitation in devices such as the resonant optical fields described in Refs. [50–52]. In contrast, prior reports [18] primarily considered changes in near-field plasmonic profiles with asymmetric plasmonic structures such as orthogonal nanorods or disk/ring dimer structures using the finite-difference time-domain (FDTD). Polarization-dependent changes in Fano resonance and thus absorption and near fields for various sizes and separations of the structures were considered. It was shown that multiple Fano resonances could be supported by larger-sized elements.

Individual spectra for a 70 nm radius Au nanoparticle in Fig. 4 at increasing RI values illustrate changes in resonance energy and bandwidth due to the underlying changes in polarizability shown in Fig. 3. The extinction features are nearly identical when calculated using Eq. (1) polarizability (solid lines) and the exact Mie theory (dotted lines) at RI values of 1.00 (blue), 1.25 (green), and 1.50 (black), respectively. The peak location for the plasmon resonance redshifts from 545 to 677 nm, and the full width at half-maximum (FWHM) increases from 67 to 93 nm as RI is increased from 1.00 to 1.50. These changes are similar to those observed experimentally. At RI of 1.50, the quadrupole plasmon resonance appears. This feature has been predicted to give diffractive coupling from quadrupole scattering in periodic arrays [44]. The rsa-CDA and Mie calculations are indistinguishable at energies less than or at resonance for smaller RI values. Differences appear as smaller incident wavelengths begin to induce quadrupole modes at higher RI. Higher RI enhances the effect as illustrated in the inset of Fig. 1. Specifically, dipole plasmon wavelength and amplitude for the RI of 1.5 gives a relative error of –0.498% and –0.588%, respectively. Quadrupole plasmon wavelength and amplitude have relative errors of 0.541% and 8.17%, respectively, at the same conditions. This indicates that approximating quadrupole polarizability with the dipole expression in Eq. (1) slightly underestimates the dipole resonance while slightly exaggerating the quadrupole. The spectral sensitivity of the photon–nanoparticle interaction to changes in RI is assessed subsequently using these two plasmon peaks.

5. FANO RESONANCE ENERGY IS MORE SENSITIVE TO CHANGES IN REFRACTIVE INDEX

Figure 5 illustrates that the Fano resonance peak energy is more sensitive to changes in the intervening dielectric than uncoupled dipole or quadrupole plasmon resonance energies. The spectra shown were from square lattices of nanoparticles calculated using the rsa-CDA at RI values of 1, 1.17, and 1.33. The inset compares redshifts in Fano (right-hand line), dipole

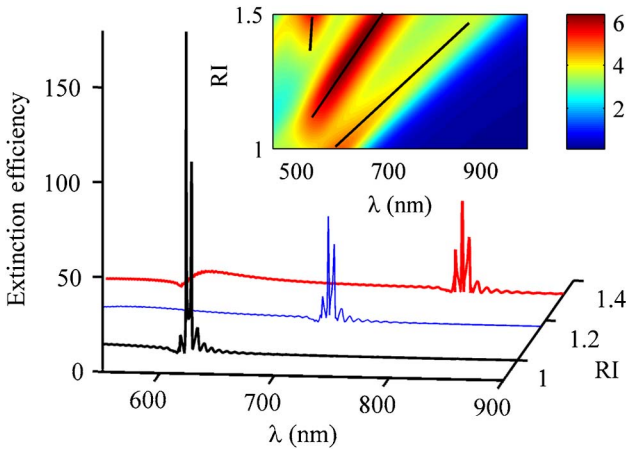

Fig. 5. Extinction spectra for a square lattice of 70 nm radius particles spaced at 600 nm with RI values of 1.00, 1.17, and 1.33 using the rsa-CDA. Inset shows spectral results for a 5×5 array of 70 nm Au particles with a lattice constant of 600 nm using the finite CDA. The value of extinction efficiency at the RI and wavelength shown appears as a color gradient.

(middle line), and quadrupole (left-hand line) peaks due to increases in RI from 1 to 1.5 (in 0.01 increments). Inset data are from a finite 5×5 array calculated using CDA and show extinction spectra magnitude in a color gradient as a function of incident wavelength (abscissa) and RI (ordinate). All lattices in Fig. 5 contain 70 nm particles spaced 600 nm apart. Incident vacuum wavelengths were calculated in 1 nm increments. The relative extinction efficiencies in the main plot exceed those in the inset since more particles are simulated. In the inset, quadrupole (left ~500 nm), dipole (middle 500–700 nm), and Fano resonance (right 600–875 nm) peaks from the 5×5 square array of particles appear at respectively lower incident energies. Each redshifts with increasing RI, albeit at successively higher rates: 150, 348, and 541 nm/RIU for the quadrupole, dipole, and Fano peaks, respectively. By comparison, Mie theory predicts an isolated 70 nm radius particle would exhibit quadrupole and dipole localized surface plasmon resonance redshifts of 71 and 224 nm/RIU, respectively. Sensitivity to changes in external dielectric constant is thus higher in all cases for arrayed nanoparticles than for random nanoparticles, and led by the Fano peak sensitivity. Enhanced spectral intensity and response of Fano resonances from photonic crystals was also explored in Ref. [22]. Far-field coupling was considered using the finite element method (FEM) in COMSOL, and a classical coupled oscillator model was discussed to explain the observed Fano resonances.

The Fano peak sensitivity using the rsa-CDA in the main plot of Fig. 5 was found to be 608.23 nm/RIU, larger than the finite array sensitivity from the inset. This is 1.5 to 14 times greater than single particle plasmon sensitivities reported previously in the literature [7]. But it is smaller than a value of 966.7 nm/RIU reported for diffractive coupling in periodic repeating chains [53]. This study reported a lattice constant in the IR band yielded a larger array sensitivity, albeit at a lower intensity. Substituting lattice constants and RI values equivalent to those in Ref. [53] into the present simulation resulted in a calculated sensitivity of 848.5 nm/RIU without optimizing array geometry. These sensitivities from far-field coupling between polarizability and in-plane scattering are also smaller than some near-field Fano resonance values reported at

1116 nm/RIU (Ref. [16]). However, detection of RI changes for near fields has a limited range of 5–15 nm from the particle surface, while far-field resonances can extend hundreds of nanometers [7].

6. RSA-CDA CAN MAXIMIZE FANO SENSITIVITY

Figure 6 illustrates use of the rsa-CDA to identify particle radii (ordinate) and lattice constants (abscissa) that maximize Fano sensitivity (color scale) to a change in RI from vacuum to 1.10. A total of 11,256 unique square lattices were simulated for particle radii from 25 to 80 nm and lattice constants from 500 to 700 nm. An 80 nm particle radius limits radiation to primarily dipolar modes. Lattice constants above 700 nm would generate greater sensitivity, but were not simulated due to decreased Fano resonance intensity at these longer wavelengths. The latter results from energy smaller than the single particle plasmon window. Sensitivity was calculated by subtracting the Fano resonance peak wavelength obtained at RI = 1.1 from that at RI = 1.0 and dividing this difference by ΔRI = 0.1. Predicted sensitivities increase from about 525 nm/RIU at 500 nm lattice constants to 700 nm/RIU at 700 nm lattice constants.

Linear aberrations that appear in the plot and deviate from this trend result from geometric configurations of the lattice from local constructive and destructive regions of scattered light [41]. These linear lines correspond to geometries of high Fano resonance intensity as will be shown in Fig. 7. This suggests intense Fano resonances can produce larger sensitivities to local environmental changes. These lines alternate from lower to higher sensitivities relative to the overall trend. Increasing RI of the dielectric intervening between embedded particles causes detectable redshifts in the resulting Fano resonance, whose frequency depends jointly on particle polarizability, α, and the lattice parameter, A, which are both functions of medium wavenumber [41,42]. Particle morphology and spacing can be independently adjusted to satisfy particular wavelength-specific applications [54].

Figure 7 illustrates that changing RI from 1.00 to 1.33 shifts the particle radii and lattice constants that maximize constructive coupling in the Fano resonance (color scale). Each colored meshpoint in each plot corresponds to the maximum calculated amplitude of extinction efficiency (i.e., the Fano resonance) obtained for one of 16,586 simulations that constitute the plots. Incident wavelength values from 400 to 1000 nm

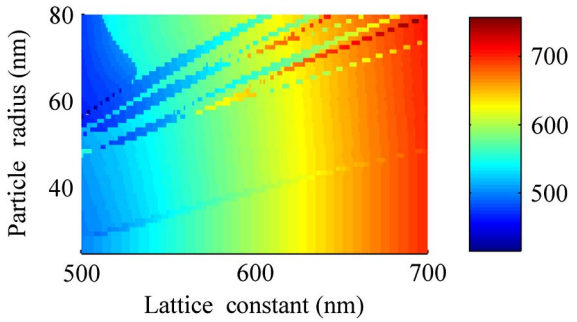

Fig. 6. Sensitivity shown by wavelength shift of Fano resonance peak wavelength per RI unit (RIU) for a given geometric combination of lattice constant and particle radius. RI change for the calculation was from 1.00 to 1.10.

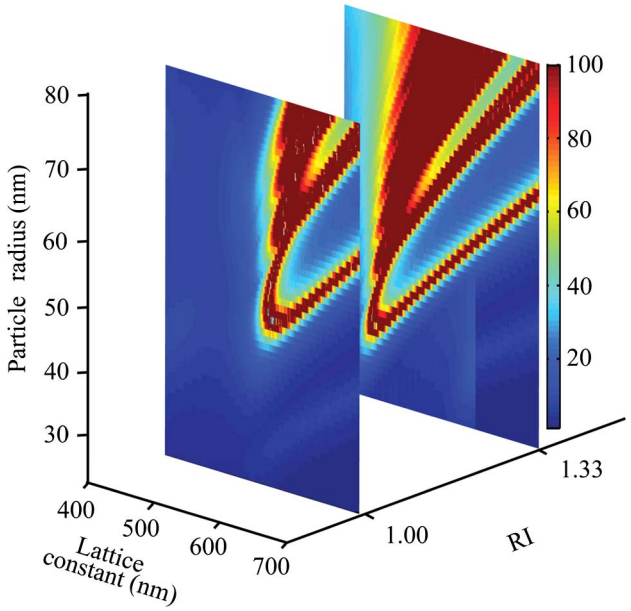

Fig. 7. Array geometries that yield extraordinary Fano resonance through constructive interference of scattered light. The color gradient shows the maximum extinction of the Fano resonance as a function of lattice constant and particle radius.

were sampled in 0.1 nm increments for arrays with lattice constants from 400 to 700 nm and particle radii from 25 to 80 nm in 1 nm increments. Values of Fano resonance intensity represented in color were truncated to a maximum of 100 to suppress a small number of more intense peaks.

Figure 7 shows that a larger window of (smaller) lattice constants and particle radii supports maximal Fano resonance intensity at larger RI values. The parabolic loci of maximum Fano intensity exhibit three changes. First, the limiting radius at which coupling produces an extraordinary peak decreases from 44 nm at RI = 1.0 to 31 nm at RI = 1.33. This decrease results from a corresponding shift in measurable particle polarizability values to lower NP radii, illustrated in Fig. 3. As RI increases, the measurable dipole resonance values apparent in Fig. 3 redshift and begin to occur at smaller radii. Equivalently, Mie theory shows that increasing the RI surrounding a single particle causes scattering to increase for a given particle.

Second, the limiting lattice constant that supports constructive Fano resonance coupling decreases as intervening RI increases: from 539 nm at RI = 1.0 to 425 nm at RI = 1.33. This seems counterintuitive since Fano resonances are not supported at vacuum wavelengths smaller than that for the plasmon resonance and the plasmon wavelength redshifts with increasing RI. However, Fig. 1 shows that the Fano wavelength occurs at a value of $D\eta$. Increasing η permits an inversely smaller value of D to support the Fano resonance at a vacuum wavelength equal to their product provided this energy remains lower than the plasmon resonance. In other words, the plasmon peak redshifts sublinearly at a slower rate than wavelength compresses linearly in proportion to increased η.

Third, the gap in the parabolas caused by destructive interference decreases as RI is increased. This results from broadening of the dipole mode for larger values of RI illustrated in Fig. 3. Since the partial derivative of polarizability

with respect to wavelength is increasingly larger than with respect to radius as RI increases, the Fano peak sweeps over the allowed constructive and destructive regions more quickly along the lattice constant, thus narrowing the gap between successive regions of constructive interference. Control over Fano resonance energy and linewidth by adjusting broad and narrow constituent resonances is analogous to coupling between multiple sub- and super-radiant modes in a hetero-oligomer structure of two different homodimers [10] and in dolmen configurations [12]. Fano resonance was shown to be independently controlled by varying structure geometry [11,13]. Control of Fano resonance resulting from light coupling between a thin film of metal nanoparticles and an array of metal nanorods was similarly considered in Ref. [17]. Layered media results were obtained from FDTD and DDA that compared favorably with experimental data, showing light transmission and local electromagnetic fields could be independently enhanced by nanostructure design.

7. FUTURE DIRECTIONS

Plasmonic nanostructures in metamaterials exhibit Fano resonances that allow light to be manipulated below the Rayleigh diffraction limit for emerging applications such as subwavelength image resolution, information transport in quantum computing [24,25], enhanced THz emission and transparency in 2D photonic crystals [26,27], and biological imaging [28,29]. Periodic plasmonic nanostructures have been combined with graphene in particular to create photodetectors [50,55–57] with increased absorption of incident light and for photocurrent devices [54,58]. Generally, metal nanostructures generate photocurrent in semiconductors and van der Waals solids from band bending in creation of a p-n junction. Fano resonant, plasmonic systems have been postulated to increase photon absorption in graphene through either direct excitation (DE) of electron hole pairs in graphene or hot electron (HE) transfer. DE is produced by absorption of incident photons by graphene that are separated by intensified plasmonic near fields within the graphene from nanostructures formed on or between graphene layer(s). HE results from zero-band gap graphene accepting electrons through direct transfer from the nanostructures' plasmon via absorption of incident light [57]. Separation of electron hole pairs in graphene occurs through electrostatic steps in potential [59]. Metallic contacts that produce such a step [60] have been incorporated to increase coverage of the graphene surface [54,61–63].

Progress in engineering band structures in semiconductors and van der Waals solids such as graphene with plasmon–photon Fano resonances has been limited to date by attention given primarily to plasmon–plasmon Fano resonances and by computational challenges and expense. Although "meta-atoms" in reported structures are often arranged periodically, occurrence of Fano resonances from interaction between plasmons and diffracted photons has been infrequent. Most analyses have considered Fano resonances from plasmon–plasmon interactions within a single "meta-atom." One exception is reported in Ref. [54], where the FEM was used to simulate field enhancements from monomers, dimers, and periodic nanowires using a few select lattice spacings to compare with experimentally measured photocurrent enhancements. This work showed nanoarchitectures optimized for specific Fano resonance wavelength tuning could be integrated with graphene for light filtering, photodetecting, etc., in a single device [54]. However, finite element and finite difference methods can obscure attribution of Fano resonant band structures arising from plasmon–photon coupling to specific effects arising from particle size, lattice constant, or RI in periodic arrays of "meta-atoms." This work supports development of photon–plasmon-coupled Fano resonant plasmonic nanostructures for graphene devices, which requires distinguishing the influence of meta-atom architecture and placement as well as influence of the local dielectric media constant across broad ranges.

8. CONCLUSION

This work distinguished effects of changes in RI, particle size, and incident energy on a Fano resonance supported by coupling between a broadband plasmon resonance and a narrowband phase-superpositioned diffractive mode. It did so using a rsa-CDA of extinction efficiency for a square lattice of dipoles. RI affected spectral features via a RI-dependent medium wavenumber that impacts nanoparticle polarizability as well as a lattice parameter that governed the frequency and energy-dependent intensity of in-plane, far-field diffraction. Particle polarizability was impacted by changes in RI and particle size. Varying RI altered the diffractive mode and Fano resonant energy. Sensitivity of the Fano resonance peak wavelength to changes in RI was increased more than 2.4-fold relative to the sensitivity of isolated nanoparticles. The sensitivities of dipole and quadrupole resonances for nanoparticles arrayed in square lattices were also larger than for isolated nanoparticles. Results from the present work support precision engineering of 2D photonic crystals to meet the requirements for adaptive electromagnetic activity and sensitivity required by next-generation optoelectronic device applications.

ACKNOWLEDGMENTS

This work was supported in part by NSF CMMI-0909749, NSF CBET 1134222, NSF ECCS-1006927, the Walton Family Charitable Support Foundation, and the University of Arkansas Foundation. D. DeJarnette performed simulations and prepared data and text for the manuscript. J. Norman performed simulations and aided in text revision. D. K. Roper directed the work and prepared and organized the final text.

REFERENCES

1. R. W. Wood, "Anomalous diffraction gratings," Phys. Rev. **48**, 928–936 (1935).
2. U. Fano, "Effects of configuration interaction on intensities and phase shifts," Phys. Rev. **124**, 1866–1878 (1961).
3. W. L. Bragg, "The specular reflection of X-rays," Nature **90**, 410 (1912).
4. P. Blake, W. Ahn, and D. K. Roper, "Enhanced uniformity in arrays of electroless plated spherical gold nanoparticles using tin presensitization," Langmuir **26**, 1533–1538 (2010).
5. W. Ahn, P. Blake, J. Schulz, M. E. Ware, and D. K. Roper, "Fabrication of regular arrays of Au nanospheres by thermal transformation of electroless-plated films," J. Vac. Sci. Technol. B **28**, 638–642 (2010).
6. G. Mie, "Contributions to the optics of turbid media, particularly of colloidal metal solutions," Ann. Phys. **25**, 377–445 (1908).
7. P. Blake, J. Obermann, B. Harbin, and D. K. Roper, "Enhanced nanoparticle response from coupled dipole excitation for plasmon sensors," IEEE Sens. J. **11**, 3332–3340 (2011).
8. D. K. Roper, W. Ahn, B. Taylor, and Y. D'Asen, "Enhanced spectral sensing by electromagnetic coupling with localized surface

plasmons on subwavelength structures," IEEE Sens. J. **10**, 531–540 (2010).
9. M. V. Rybin, A. B. Khanikaev, M. Inoue, K. B. Samusev, M. J. Steel, G. Yushin, and M. F. Limonov, "Fano resonance between Mie and Bragg dcattering in photonic crystals," Phys. Rev. Lett. **103**, 023901 (2009).
10. A. Artar, A. A. Yanik, and H. Altug, "Directional double Fano resonances in plasmonic hetero-oligomers," Nano Lett. **11**, 3694–3700 (2011).
11. B. Gallinet and O. J. F. Martin, "Ab initio theory of Fano resonances in plasmonic nanostructures and metamaterials," Phys. Rev. B **83**, 235427 (2011).
12. B. Gallinet and O. J. F. Martin, "Relation between near-field and far-field properties of plasmonic Fano resonances," Opt. Express **19**, 22167–22175 (2011).
13. B. Gallinet and O. J. F. Martin, "Influence of electromagnetic interactions on the line shape of plasmonic Fano resonances," ACS Nano **5**, 8999–9008 (2011).
14. A. Christ, Y. Ekinci, H. H. Solak, N. Gippius, S. G. Tikhodeev, and O. J. F. Martin, "Controlling the Fano interference in a plasmonic lattice," Phys. Rev. B **76**, 201405 (2007).
15. Y. Francescato, V. Giannini, and S. Maier, "Plasmonic systems unveiled by Fano resonances," ACS Nano **6**, 1830–1838 (2012).
16. F. Hao, P. Nordlander, Y. Sonnefraud, P. V. Dorpe, and S. Maier, "Tunability of subradiant dipolar and Fano-type plasmon resonances in metallic ring/disk cavities: implications for nanoscale optical sensing," ACS Nano **3**, 643–652 (2009).
17. Z. K. Zhou, X. N. Peng, Z. J. Yang, Z. S. Zhang, M. Li, X. R. Su, Q. Zhang, X. Shan, Q. Q. Wang, and Z. Zhang, "Tuning gold nanorod-nanoparticle hybrids into plasmonic Fano resonance for dramatically enhanced light emission and transmission," Nano Lett. **11**, 49–55 (2011).
18. N. Verellen, Y. Sonnefraud, H. Sobhani, F. Hao, V. V. Moshchalkov, P. V. Dorpe, P. Nordlander, and S. A. Maier, "Fano resonances in individual coherent plasmonic nanocavities," Nano Lett. **9**, 1663–1667 (2009).
19. T. G. Habteyes, S. Dhuey, S. Cabrini, P. J. Schuck, and S. R. Leone, "Theta-shaped plasmonic nanostructures: bringing "dark" multipole plasmon resonances into action via conductive coupling," Nano Lett. **11**, 1819–1825 (2011).
20. B. luk'yanchuk, N. I. Zheludev, S. A. Maier, N. J. Halas, P. Nordlander, H. Giessen, and C. T. Chong, "The Fano resonance in plasmonic nanostructures and metamaterials," Nat. Mater. **9**, 707–715 (2010).
21. V. Giannini, Y. Francescato, H. Amrania, C. C. Phillips, and S. A. Maier, "Fano resonances in nanoscale plasmonic systems: a parameter-free modeling approach," Nano Lett. **11**, 2835–2840 (2011).
22. S. R. K. Rodriguez, A. Abass, B. Maes, O. T. A. Janssen, G. Vecchi, and J. Gómez Rivas, "Coupling bright and dark plasmonic lattice resonances," Phys. Rev. X **1**, 021019 (2011).
23. S. H. Mousavi, A. B. Khanikaev, and G. Shvets, "Optical properties of Fano-resonant metallic metasurfaces on a substrate," Phys. Rev. B **85**, 155429 (2012).
24. R. D. Artuso and G. W. Bryant, "Hybrid quantum dot-metal nanoparticle systems: connecting the dots," Acta Phys. Pol. A **122**, 289–293 (2012).
25. D. E. Chang, A. S. Sørensen, P. R. Hemmer, and M. D. Lukin, "Quantum optics with surface plasmons," Phys. Rev. Lett. **97**, 053002 (2006).
26. X. Lu, J. Han, and W. Zhang, "Resonant terahertz reflection of periodic arrays of subwavelength metallic rectangles," Appl. Phys. Lett. **92**, 121103 (2008).
27. S. Park, K. H. Jin, M. Yi, J. C. Ye, J. Ahn, and K. Jeong, "Enhancement of terahertz pulse emission by optical nanoantenna," ACS Nano **6**, 2026–2031 (2012).
28. P. K. Jain, X. Huang, I. H. El-Sayed, and M. A. El-Sayed, "Noble metals on the nanoscale: optical and photothermal properties and some applications in imaging, sensing, biology, and medicine," Acc. Chem. Res. **41**, 1578–1586 (2008).
29. M. Hu, J. Chen, Z. Li, L. Au, G. V. Hartland, X. Li, M. Marquez, and Y. Xia, "Gold nanostructures: engineering their plasmonic properties for biomedical applications," Chem. Soc. Rev. **35**, 1084–1094 (2006).
30. R. B. Dunbar, H. C. Hessee, D. S. Lembke, and L. Schmidt-Mende, "Light-trapping plasmonic nanovoid arrays," Phys. Rev. B **85**, 035301 (2012).
31. C. P. Huang, X. G. Yin, Y. Zhang, S. B. Wang, Y. Y. Zhu, H. Liu, and C. T. Chan, "Deep subwavelength Fabry–Perot-like resonances in a sandwiched reflection grating," Phys. Rev. B **85**, 235410 (2012).
32. S. Linden, J. Kuhl, and H. Giessen, "Controlling the interaction between light and gold nanoparticles: selective suppression of extinction," Phys. Rev. Lett. **86**, 4688–4691 (2001).
33. N. N. Lal, H. Zhou, M. Hawkeye, J. K. Sinha, P. N. Bartlett, G. A. J. Amaratunga, and J. J. Baumberg, "Using spacer layers to control metal and semiconductor absorption in ultrathin solar cells with plasmonic substrates," Phys. Rev. B **85**, 245318 (2012).
34. R. Catchpole and A. Polman, "Plasmonic solar cells," Opt. Express **16**, 21793–21800 (2008).
35. P. Offermans, M. C. Schaafsma, S. R. K. Rodrigue, Y. Zhang, M. Crego-Calama, S. H. Brongersma, and J. Gomez Rivas, "Universal scaling of the figure of merit of plasmonic sensors," ACS Nano **5**, 5151–5157 (2011).
36. T. J. Davis, D. E. Gómez, and K. C. Vernon, "Interaction of molecules with localized surface plasmons in metallic nanoparticles," Phys. Rev. B **81**, 045432 (2010).
37. H. Chen, L. Shao, Y. C. Man, C. Zhao, J. Wang, and B. Yang, "Fano resonance in (gold core)–(dielectric shell) nanostructures without symmetry breaking," Small **8**, 1503–1509 (2012).
38. H. Chen, L. Shao, T. Ming, K. C. Woo, Y. C. Man, J. Wang, and H. Q. Lin, "Observation of the Fano resonance in gold nanorods supported on high-dielectric-constant substrates," ACS Nano **5**, 6754–6763 (2011).
39. Y. Zhao and A. Alu, "Manipulating light polarization with ultrathin plasmonic metasurfaces," Phys. Rev. B **84**, 205428 (2011).
40. N. Papasimakis, Z. Luo, Z. X. Shen, F. De Angelis, E. Di Fabrizio, A. E. Nikolaenko, and N. I. Zheludev, "Graphene in a photonic metamaterial," Opt. Express **18**, 8353–8359 (2010).
41. D. DeJarnette, J. Norman, and D. K. Roper, "Spectral patterns underlying polarization-enhanced diffractive interference are distinguishable by complex trigonometry," Appl. Phys. Lett. **101**, 183104 (2012).
42. D. DeJarnette, D. K. Roper, and B. Harbin, "Geometric effects on far-field coupling between multipoles of nanoparticles in square arrays," J. Opt. Soc. Am. B **29**, 88–100 (2012).
43. P. G. Etchegoin, E. C. Le Ru, and M. Meyer, "An analytic model for the optical properties of gold," J. Chem. Phys. **125**, 164705 (2006).
44. A. B. Evlyukhin, C. Reinhardt, U. Zywietz, and B. N. Chichkov, "Collective resonances in metal nanoparticle arrays with dipole-quadrupole interactions," Phys. Rev. B **85**, 245411 (2012).
45. K. L. Kelly, E. Coronado, L. L. Zhao, and G. C. Schatz, "The optical properties of metal nanoparticles: the influence of size, shape, and dielectric environment," J. Phys. Chem. B **107**, 668–677 (2003).
46. Y. Chu, E. Schonbrun, T. Yang, and K. B. Crozier, "Experimental observation of narrow surface plasmon resonances in gold nanoparticle arrays," Appl. Phys. Lett. **93**, 181108 (2008).
47. S. Zou and G. Schatz, "Narrow plasmonic/photonic extinction and scattering line shapes for one and two dimensional silver nanoparticle arrays," J. Chem. Phys. **121**, 12606–12612 (2004).
48. E. Simsek, "Effective refractive index approximation and surface plasmon resonance modes of metal nanoparticle chains and arrays," PIERS Online **5**, 629–632 (2009).
49. T. Jensen, L. Kelly, A. Lazarides, and G. C. Schatz, "Electrodynamics of noble metal nanoparticles and nanoparticle clusters," J. Cluster Sci. **10**, 295–317 (1999).
50. Y. Liu, R. Cheng, L. Liao, H. Zhou, J. Bai, G. Liu, L. Liu, Y. Huang, and X. Duan, "Plasmon resonance enhanced multicolour photodetection by graphene," Nat. Commun. **2**, 579 (2011).
51. S. F. Shi, X. Xu, D. C. Ralph, and P. L. McEuen, "Plasmon resonance in individual nanogap electrodes studied using graphene nanoconstrictions as photodetectors," Nano Lett. **11**, 1814–1818 (2011).
52. A. Gopalakrishnan, M. Malerba, S. Tuccio, S. Panaro, E. Miele, M. Chirumamilla, S. Santoriello, C. Dorigoni, A. Giugni, R. P. Zaccaria, C. Liberale, F. De Angelis, L. Razzari, R. Krahne, A. Toma, G. Das, and E. Di Fabrizio, "Nanoplasmonic structures

for biophotonic applications: SERS overview," Ann. Phys. **524**, 620–636 (2012).
53. B. Bai, X. Li, I. Vartiainen, A. Lehmuskero, G. Kang, J. Turunen, M. Kuittinen, and P. Vahimaa, "Anomalous complete opaqueness in a sparse array of gold nanoparticle chains," Appl. Phys. Lett. **99**, 081911 (2011).
54. T. J. Echtermeyer, L. Britnell, P. K. Jasnos, A. Lombardo, R. V. Gorbachev, A. N. Grigorenko, A. K. Geim, A. C. Ferrari, and K. S. Novoselov, "Strong plasmonic enhancement of photovoltage in graphene," Nat. Commun. **2**, 458 (2011).
55. F. Xia, T. Mueller, Y. Lin, A. Valdes-Garcia, and P. Avouris, "Ultrafast graphene photodetector," Nat. Nanotechnol. **4**, 839–843 (2009).
56. G. Konstantatos, M. Badioli, L. Gaudreau, J. Osmond, M. Bernechea, F. P. G. de Arquer, F. Gatti, and F. H. L. Koppens, "Hybrid graphene–quantum dot phototransistors with ultrahigh gain," Nat. Nanotechnol. **7**, 363–368 (2012).
57. Z. Fang, Z. Liu, Y. Wang, P. M. Ajayan, P. Nordlander, and N. J. Halas, "Graphene-antenna sandwich photodetector," Nano Lett. **12**, 3808–3813 (2012).
58. C. X. Guo, H. B. Yang, Z. M. Sheng, Z. S. Lu, Q. L. Song, and C. M. Li, "Layered graphene/quantum dots for photovoltaic devices," Angew. Chem., Int. Ed. **49**, 3014–3017 (2010).
59. S. Mai, S. V. Syzranov, and K. B. Efetov, "Photocurrent in a visible-light graphene photodiode," Phys. Rev. B **83**, 033402 (2011).
60. T. Mueller, F. Xia, M. Freitag, J. Tsang, and P. Avouris, "Role of contacts in graphene transistors: a scanning photocurrent study," Phys. Rev. B **79**, 245430 (2009).
61. A. Gutes, B. Hsia, A. Sussman, W. Mickelson, A. Zettl, C. Carraro, and R. Maboudian, "Graphene decoration with metal nanoparticles: towards easy integration for sensing applications," Nanoscale **4**, 438–440 (2012).
62. Z. Fang, Y. Wang, Z. Liu, A. Schlather, P. M. Ajayan, F. H. L. Koppens, P. Nordlander, and N. J. Halas, "Plasmon-induced doping of graphene," ACS Nano **6**, 10222–10228 (2012).
63. C. Y. Liu, K. Liang, C. C. Chang, and Y. Tzeng, "Effects of plasmonic coupling and electrical current on persistent photoconductivity of single-layer graphene on pristine and silver nanoparticle-coated SiO_2/Si," Opt. Express **20**, 22934–22952 (2012).